

S. A. Stanier¹ and D. J. White²

Improved Image-Based Deformation Measurement in the Centrifuge Environment

REFERENCE: Stanier, S. A. and White, D. J., "Improved Image-Based Deformation Measurement in the Centrifuge Environment," *Geotechnical Testing Journal*, Vol. 36, No. 6, 2013, pp. 1–14, doi:10.1520/GTJ20130044. ISSN 0149-6115.

ABSTRACT: This paper describes a new apparatus and techniques for performing deformation measurements using particle image velocimetry in the centrifuge environment. The new system includes camera, lighting, and control equipment that facilitates image capture at least 30 times faster than that in legacy systems. Methods for optimizing the addition of artificial seeding on the exposed plane of a geotechnical model are also set out. These techniques ensure that the precision of the deformation calculations is optimized even in models with multiple layers of different soils, fully harnessing the method's capabilities. An example application of a flat footing penetrating sand overlying clay is used to illustrate the performance of the equipment and the artificial seeding optimization technique. Deformation fields at the point of peak resistance during punch-through are presented in the form of vector fields, normalized displacement contours, and shear strain contours. It is shown that the advances in equipment and artificial seeding allow both macroscopic and grain-scale deformation features to be identified. These analyses highlight not only the benefits of the new technology, but also the need for carefully optimized experimental procedures to maximize the measurement precision.

KEYWORDS: centrifuge, particle image velocimetry, PIV, texture, precision, optimization, deformation measurement

Nomenclature

ASR = artificial seeding ratio

D = diameter

D₅₀ = diameter of median particle size

HDD = hard disk drive

H_s = Height of sand layer

I_D = relative density

$\overline{I_{px}}$ = mean pixel intensity of all patches

$\overline{I_{px,i=1}}$ = mean pixel intensity of first image with no seeding

$\overline{I_{px,i=n}}$ = mean pixel intensity of last image with saturated seeding

L = patch size in pixels

Mpx = mega-pixel

N = number of measurement points

PCI = peripheral component interconnect

s = PIV analysis patch spacing

s_{u0} = undrained shear strength at layer surface

t = time

V = velocity

USB = universal serial bus

V_{max} = maximum velocity

W_{pixel} = image width in pixels

γ'_s = effective unit weight of sand

γ = engineering shear strain

γ_{max} = maximum engineering shear strain

δ = displacement

ρ = undrained shear strength gradient

ρ_{px} = standard error of displacement measurement in pixels

ρ_n = normalized standard error

$\rho_{n-upper}$ = normalized upper bound error estimator

$\overline{\sigma_{I_p}}$ = mean standard deviation of pixel intensity of all patches

φ_{cv} = critical state friction angle

ψ = dilation angle

Introduction

Most geotechnical physical modeling facilities feature a system of image capture and analysis in order to provide measurements of

Manuscript received March 13, 2013; accepted for publication July 29, 2013; published online September 13, 2013.

¹Research Associate, Centre for Offshore Foundation Systems, Univ. of Western Australia, M053 Fairway, Crawley, WA 6009, Australia (Corresponding author), e-mail: sam.stanier@uwa.edu.au

²Winthrop Professor, Centre for Offshore Foundation Systems, Univ. of Western Australia, M053 Fairway, Crawley, WA 6009, Australia.

deformation fields. The purpose of this paper is to describe new techniques developed for a drum centrifuge but applicable in other experimental environments. The system includes various advances beyond the state of the art described previously (White et al. 2003). With the use of a new and improved apparatus and software system, improved measurement performance is achieved. This results in a step forward in measurement utility: small particle-scale localization features can be detected within large-scale observations of boundary value problems, allowing both micro- and macro-deformation patterns to be quantified simultaneously.

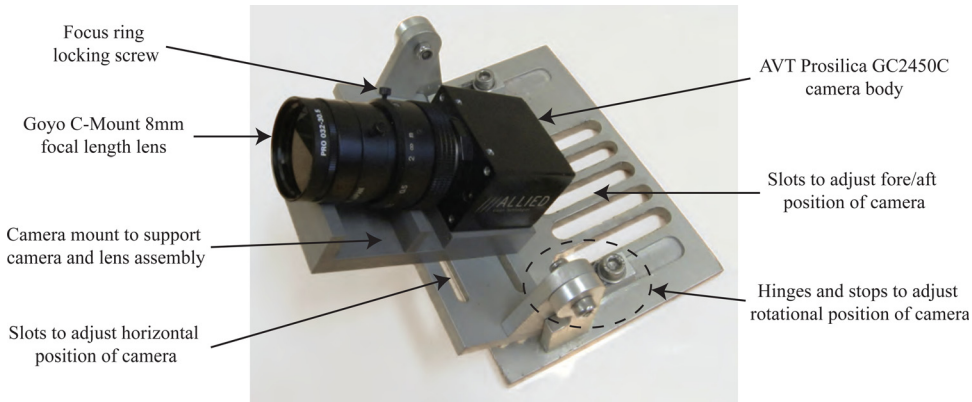


FIG. 1—AVT ProSilica GC2450C camera and mount.

First, the new apparatus is described. Second, a simple procedure to ensure that the target soil will yield optimum precision when subjected to particle image velocimetry (PIV) analysis is proposed. Finally, an example application is used to demonstrate some of the advantages of the new system and the precision optimization procedure. This example investigates the mechanism of punch-through of a flat footing on sand overlying clay, showing the detection of small localization features.

Background

Techniques for the measurement of deformations in geotechnical models have developed significantly over the past 40 years. Early studies by Butterfield et al. (1970) and Andrawes and Butterfield (1973) reported the use of stereo photogrammetry, in which individual particle movements, as seen in stereo pair photographs, are measured manually. The recent introduction of digital technology has removed the need for painstaking manual film measurements. The technique of PIV (also known as digital image correlation) has now been widely applied across many branches of engineering (Raffel et al. 2007; Pan et al. 2009; Sutton et al. 2009). The use of PIV and photogrammetry to measure soil displacement in small-scale physical models has led to a significant increase in measurement accuracy and precision relative to previously utilized techniques (White et al. 2003). Furthermore, the number of measurement points available in the analysis process has become a function of discretization (patch size) rather than the number of identifiable features (e.g., target markers) on an exposed plane of the model.

The elimination of target markers significantly reduces model preparation time, and the semi-automated nature of PIV computations has made the analysis process far less onerous. As a result, hundreds of published studies in the past 10 years have used PIV or other comparable systems to observe deformations in geotechnical physical models. The flexibility of image analysis has allowed it to be used to measure displacements in a wide range of physical model systems, at both $1g$ and ng , and also in the field (see reviews by White [2008] and Gaudin et al. [2010a]).

White et al. (2003) demonstrated that geotechnical PIV measurement precision is a function of the image texture of the disre-

tized analysis domain. In models incorporating fine-grained soils such as clays, artificial texture is added to the exposed plane of the model using modeling flock (White et al. 2005) or dyed sand (Take and Bolton 2011). Similarly, for transparent soils, minute titanium oxide seeding particles are added to provide image texture (Stanier et al. 2012). Conversely, for models incorporating coarse-grained soils such as sands, the natural variation of pixel intensity caused by the range of colors and shadows amongst the individual sand grains is often relied on to provide the texture required in the PIV analysis. However, to date, little attention has been paid to how this image texture may be optimized to ensure that measurement precision is maximized.

In this paper, the development of a new generation of displacement measurement apparatuses is discussed. It has been used in the University of Western Australia (UWA) drum centrifuge, which is 1.2 m in diameter, measured to the inner surface of the ring channel, and features independent rotating drives for the main channel and the central tool table. Small strongboxes with transparent side windows are located in the drum channel when performing tests involving image analysis. Further details of the drum centrifuge, as commissioned in 1998, are provided by Stewart et al. (1998).

New Apparatus

Hardware

Camera—The camera is a small-format, five-megapixel (Mpx) resolution machine vision camera (Allied Vision Technologies ProSilica GC2450C) coupled with a Goya C-Mount 8-mm focal length lens that has the facility to lock the aperture and focal rings for security during flight. The camera is shown on its mount in Fig. 1; the mount allows for up to two cameras to be mounted with fixed angles and lateral positioning while looking perpendicularly at the target window. This device was chosen principally for two features: the charge-coupled device (CCD) sensor and the global shutter capture mode.

Firstly, the CCD sensor affords greater uniformity in the recorded image than a similar-resolution complementary metal-

TABLE 1—Summary of capabilities of AVT Prosilica GC2450C camera versus Canon S40/50 camera previously used in drum centrifuge by [White et al. \(2005\)](#).

| Feature | ProSilica GC2450C | Canon S40/50 | Benefit |
|----------------------------------|--|---|---|
| Image resolution, million pixels | 5 | 3.8/5 | Comparable resolution |
| Maximum image capture rate, Hz | 15 | 0.5 | Factor of improvement of 30 |
| Image capture capacity | Limited by hard disk drive capacity on logging computer | Limited by onboard CompactFlash card size | Essentially limitless data can be captured by the new system |
| Lens assembly | Goyo C-Mount 8-mm focal length 5-Mpx lens with aperture and focal ring locks | Flexible zoom lens assembly with 35 - to 105-mm focal length | No moving parts in C-series lens should lead to improved stability at g |
| Camera size and format | 46 mm by 33 mm by 105 mm (width by height by length including lens) | 112 mm by 58 mm by 62 mm (width by height by length with lens extended) | Potential to use multiple cameras side by side in confinement of drum channel (e.g., to provide both close-up and wide-angle views of a single event) |
| Live preview | Available via gigabit LAN connection and software interface | Unavailable | Allows checking of camera view in flight before testing |
| Live setting adjustment | Available via gigabit LAN connection and software interface | Unavailable | Allows adjustment of camera settings (exposure period, sensitivity, color balance, etc.) in flight |
| Real-time image capture control | Available via gigabit LAN connection and software interface or RS232 port on camera body | Image capture triggered by shutter weight at a predefined g level | Images can be captured at any point in time at any chosen capture rate up to the maximum frame rate |

oxide semiconductor (CMOS) sensor. In a CCD sensor, a single amplifier is used to convert the charge of each of the pixels on the sensor into an output intensity, whereas in a CMOS sensor, each pixel has its own amplifier. Manufacturing amplifiers with identical responses is extremely difficult, so images recorded by CMOS sensors are generally less uniform than those recorded by a CCD sensor. In PIV analysis where a patch of soil is tracked from point A to point B, this can translate to erroneous drift in the apparent intensities within a patch, which occludes the peak of the correlation function used in the PIV computations, leading to reduced precision.

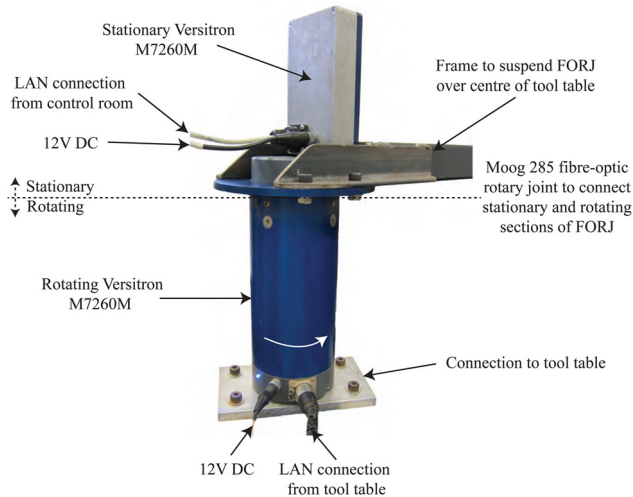
Secondly, a global shutter is required to record a true snapshot of the physical model. A global shutter camera controls the time of exposure of each pixel individually, and thus can execute capture of the charge of all pixels simultaneously. In contrast, a rolling shutter progressively scans the charge of each of the pixels in a line-by-line fashion, so that some time elapses between recording of the charge in the first and last pixels. This can cause distortions of rapidly translating rigid bodies within the recorded image. With reference to a PIV analysis where a patch of soil is tracked from point A to point B, this could lead to errors in the computed initial and final positions of the patch, leading to reduced positional accuracy.

Table 1 compares the new camera with a previous model used at UWA ([White et al. 2005](#)) that is typical of the cameras used in other geotechnical image analysis studies. The new form of camera provides significant advantages over the previous generation of camera used. Notably, the maximum frame rate is considerably faster, which allows the investigation of rapid phenomena such as dynamic penetration events or earthquake shaking. The other key advantage of the new camera is the gigabit local area network (LAN) interface. When coupled with control software in the form

of a custom LabVIEW virtual instrument (described later), this allows control of the camera settings, “live preview” of the camera field of view, and remote capture and storage of data.

High-speed camera systems with far higher image capture rates have been previously employed at other centers involved in earthquake modeling ([Okamura et al. 2001](#); [Knappett et al. 2006](#); [Cilingir and Madabhushi 2010](#)). However, the resolution of these systems is limited to only ~ 1 Mpx. The latest high-speed cameras (such as the MotionBLITZ EoSens mini used at the University of Cambridge [Haigh, personal communication, 2013], which can capture 3-Mpx images at up to 523 Hz) combine fast image capture rates with high resolution. However, the maximum capture rate can be sustained at full resolution only for short time periods (typically only a few seconds), until the internal camera memory buffer is filled. The maximum continuous (long-term) frame rate is limited by the maximum data throughput of the communications protocol (as with the system described here). The choice of camera should consider the predominant intended purpose of the apparatus: a high-speed camera is most appropriate for the observation of dynamic events of short duration (e.g., earthquake simulation), whereas a camera similar to that employed here is better suited for the observation of phenomena with slower displacement rates over longer durations (e.g., foundation penetration).

Lighting—In the previous system at UWA, a tungsten halogen lamp was used to illuminate the exposed plane of the test chamber. In the new system, a pair of light-emitting diode (LED) panels are used (CCS Industries Ltd., Model No. LDL2-266X30SW-WD). This offers numerous advantages. Firstly, each panel has an emitting surface of 266 mm by 30 mm, thus providing a more disperse and uniform light. The LED panels also have

FIG. 2—*FORJ setup on top of drum centrifuge tool table.*

relatively low power consumption (maximum of 21 W per unit at 24 V) and a far lower operating temperature of $\sim 40^{\circ}\text{C}$, versus $\sim 500^{\circ}\text{C}$ for the tungsten halogen lamp. This allows for longer operational periods, which may be required for long-term tests. The lack of a filament in the LEDs also makes the panels far more robust and reliable than the tungsten halogen bulbs previously used. Lastly, diffusing and polarizing filters are available for the LED panels, which can be used to reduce regions of overexposure and glare in recorded images.

Lighting and Camera Power Supply Unit—The camera and LED panels are powered by a power supply unit (PSU) that has a LAN interface allowing a TCP/IP link to control the brightness of the two LED panels independently, in flight (model: Gardasoft RT220). This controller allows stroboscopic or synchronous illumination with event-based or triggered image capture via a link joining the PSU, the camera's RS232 port, and

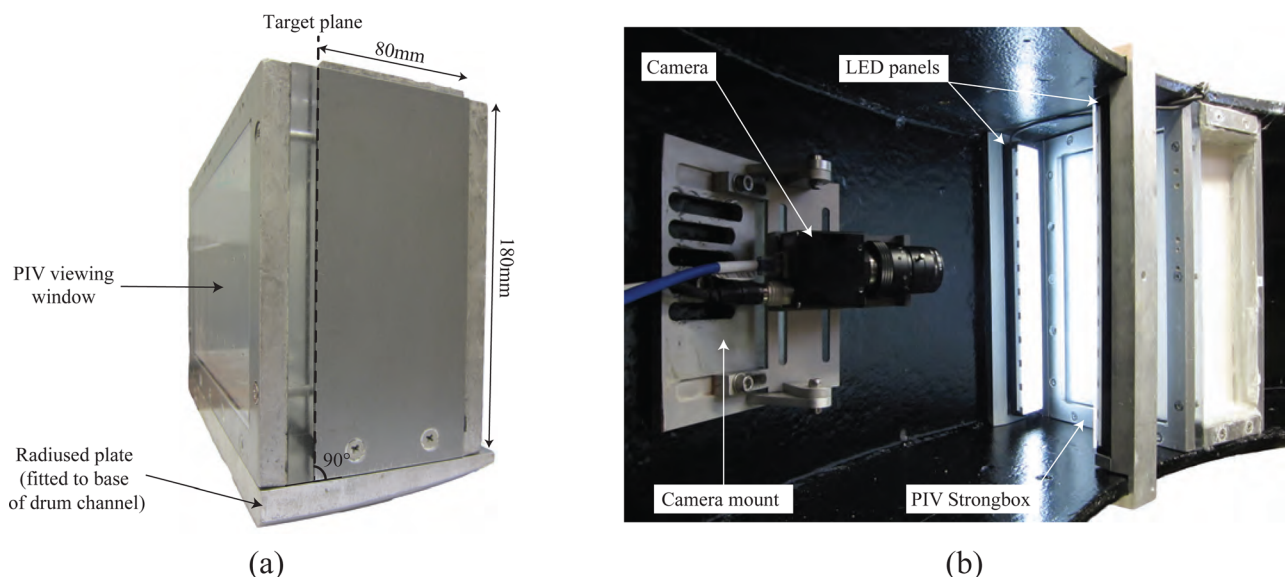
the DigiDAQ data logging system employed at UWA (see Gaudin et al. 2010b).

Fiber-Optic Rotary Joint—To maximize the frame rate, a gigabit LAN connection from the centrifuge is used, passing through a fiber-optic rotary joint (FORJ) (Moog 285) located above the tool table of the drum centrifuge (Fig. 2). On either side of this FORJ are Versitron M7260M 10/100/1000 BASE-T to 1000 BASE-X media converters, which convert the LAN connection to a fiber-optic connection and then back to a LAN connection on either side of the FORJ. A gigabit network switch is provided on the tool table, and a gigabit Ethernet port is used on the logging computer to complete the network. This system allows a transmission bandwidth of up to 100 megabytes per second, allowing images to be captured at the maximum frame rate of the camera (15 Hz).

Particle Image Velocimetry Strongbox Mounting—When image analysis tests are performed in the UWA drum centrifuge, modular strongboxes of varying thickness (80-mm to 160-mm sample width) are mounted in the drum channel. These boxes rest on a curved mounting plate with the same outer radius as the base of the drum centrifuge channel [Fig. 3(a)]. On the top of the plate, a chord has been machined that is perpendicular to the tool on the actuator. This provides a flat surface to which the strongboxes can be mounted, which ensures that the radial actuator arm moves parallel with the transparent window. Figure 3(b) shows the apparatus assembled in the drum centrifuge channel, with the strongbox mounted on the radiused plate and the camera aligned perpendicularly to the transparent window.

Software

Camera—Interface software has been developed that uses LabVIEW to control the camera (Fig. 4). The NI-IMAQdx vision

FIG. 3—(a) *The new PIV strongbox mounting scheme.* (b) *The PIV apparatus in situ within the drum centrifuge channel.*

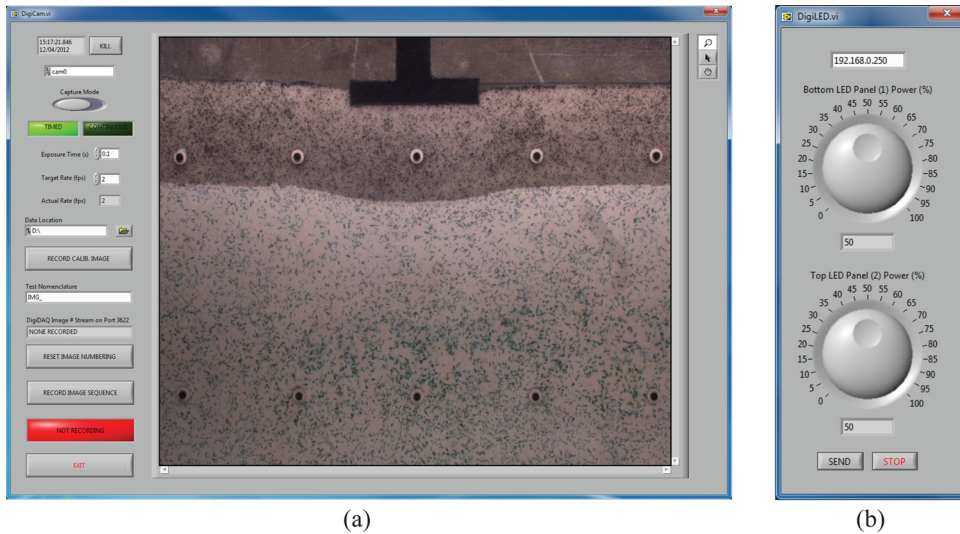


FIG. 4—Screenshots of the (a) camera control software and (b) lighting control software.

acquisition driver package facilitates communication between the software and the camera using the GigE Vision interface, which is an industry-standard communications protocol for machine vision cameras.

Within the user interface, exposure times and image capture rates can be adjusted and live view of the output of the captured images is displayed in real time. The current image number is stored within the image filename and is also streamed via a TCP/IP connection to the DigiDAQ data logging system such that a millisecond-resolution time stamp is recorded for each image captured. This allows the imaging data stream to be synchronized precisely with the other instrument data streams.

Lighting—LabVIEW software controls the LED panels using the TCP/IP communications protocol over the LAN connection provided by the FORJ; a screenshot of the control software is shown in Fig. 4(b). This facility is extremely important because it allows the brightness of the imaged soil to be varied over a continuous range, allowing the optimal image texture to be achieved. A disadvantage of fluorescent lights—relative to LEDs—is that the brightness cannot be so easily controlled.

System Cost

The total cost of the system described (excluding workshop and software development costs) was ~\$12,000 (USD). The breakdown of costs is as follows: FORJ system, ~\$5000; camera and lens assembly, ~\$4500; LED panels and PSU, ~\$2500.

Optimization of Soil Texture

To maximize the precision of PIV measurements of soil displacements, allowing the full capabilities of the apparatus to be harnessed, the spatial variation in pixel intensity should be optimized across the images. Take (2003) and White and Take (2005) note that soil image texture can be quantified by the standard deviation

of pixel intensities in any particular image patch being tracked. A larger standard deviation leads to higher precision of the PIV measurement. Thus, maximizing image texture is of critical importance to the precision of PIV analyses of geotechnical problems.

When modeling using fine-grained soils such as kaolin clay, which are typically uniformly colored, texture needs to be generated artificially by seeding the exposed plane of the model. This is often achieved with the plastic flock powder made for landscape modeling (White et al. 2005) or with dyed sand (Take and Bolton 2011).

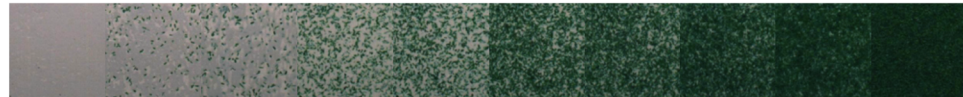
When modeling using coarse-grained soils, such as sand, the differing colors and intergrain shadows of the individual particles often create enough texture for successful PIV, without the need for additional seeding. However, some sands, such as the Dog's Bay carbonate sand used in the original calibration of GeoPIV by White et al. (2003), provide better natural texture than other sands such as the super-fine silica sand more often utilized in research at UWA. The grains of this sand are partly transparent, which means the individual grains are less distinguishable and the variations in illumination caused by interparticle shadows are reduced. Thus, there is an opportunity to improve the image texture of such sands through artificial seeding of the exposed plane of the model in the same way that is routinely employed for fine-grained soils.

In spite of the acknowledged importance of image texture to PIV precision, little attention has been paid to quantifying and optimizing the image texture attainable by artificially seeding the exposed planes of models involving either fine-grained or coarse-grained soils. To address this, a simple method of image texture optimization has been developed that can be routinely performed using a sacrificial sample, prior to commencement of the main scheme of testing of a project.

Experimental Optimization Procedure

The proposed method involves initially setting up the PIV apparatus in the same form to be used for the main scheme of testing. The test chamber is then filled with the soil to be used in the

Kaolin clay (seeded with green modelling flock):



Silica sand (seeded with dyed black sand):

 $ASR=0$

No Seeding

Increasing Artificial Seeding Ratio

 $ASR=1$

Saturated Seeding

FIG. 5—Thumbnail of the full range of ASRs observed in the texture-optimization process for both kaolin and silica sand samples.

investigation, and the brightness of the lighting system and exposure period of the camera are calibrated to give uniform exposure over the field of view for the virgin material. Artificial texture is then added to the exposed plane in stages by evenly applying small amounts of seeding material until the exposed plane is saturated with the material. An image of the model is taken at each stage, allowing PIV analysis of apparent image displacements to be performed. This entails performing a PIV analysis comparing an image with a duplicate image. This synthetic comparison allows the precision errors to be estimated from the apparent displacement. This analysis can be performed for a range of patch sizes (characterized by their width L) at the same time as the computation of other metrics, such as the mean and standard deviation of pixel intensities in each of the patches.

In this case, samples of both consolidated kaolin and dense super-fine silica sand were subjected to the proposed procedure to demonstrate its function, with 10 stages of seeding being assessed for each sample. To seed the samples, plastic modeling flock was used for the kaolin sample and dyed sand was used for the sand sample. In this instance, green modeling flock and black dyed sand were used because these contrasting colors allowed visual differentiation of the sand and clay layers in other models involving multilayered strata.

Optimization Analysis

The 10 images of each sample, representing the full spectrum of potential seeding densities, were analyzed in conjunction with GeoPIV (White and Take 2002). In this implementation, PIV patches with side lengths of 25, 50, and 100 pixels were considered, which broadly represent fine, medium, and coarse discretization of the problem. The same mesh, comprising 230 100-pixel patches, 920 50-pixel patches, and 3680 25-pixel patches, was used to analyze the kaolin clay and silica sand calibration images. The image scale was approximately 9.65 pixels/mm.

Using these calibration data, the mean pixel intensity \bar{I}_{px} of all of the patches in each of the images was calculated. The first image (no seeding) and the last image (saturated seeding) from the calibration process were then used to define bounding values for the mean pixel intensities, $\bar{I}_{px,i=1}$ and $\bar{I}_{px,i=n}$, that were subsequently used to calculate an artificial seeding ratio (ASR).

$$ASR = \frac{(\bar{I}_{px} - \bar{I}_{px,i=1})}{(\bar{I}_{px,i=n} - \bar{I}_{px,i=1})} \quad (1)$$

This yields values of the ASR that lie in the range of zero to unity, with zero indicating no seeding and unity indicating saturated seeding. The formulation of the ratio means that it is irrelevant whether the seeding used is lighter or darker than the background soil, as the ASR simply provides an indication of seeding saturation. Figure 5 presents thumbnails of the full range of ASRs for both samples.

The images were then self-compared using GeoPIV (White et al. 2003) with the resulting standard error ρ_{px} , providing an indication of the precision of the PIV calculations. The optimal ASR is identified by the minimum standard error, allowing the corresponding image to be used as a template to be matched when applying seeding to samples in the main investigation. The ASR of the actual test samples can be checked for similarity to the optimum value identified during the texture-optimization process by using Eq 1 in conjunction with the same values of $\bar{I}_{px,i=1}$ and $\bar{I}_{px,i=n}$ that were used to determine the optimum ASR.

Figures 6(a) and 6(b) are plots of the normalized seeding ratio for the kaolin clay and silica sand samples, respectively. As seeding is added to the exposed plane, the mean standard deviation of pixel intensities $\bar{\sigma}_{px}$ increases to a peak at normalized seeding ratios in the range of 0.4 to 0.6. The mean standard deviation then decreases at higher normalized seeding ratios, as the seeding begins to saturate the exposed plane.

Optimum PIV tracking precision occurs where the standard deviation of pixel intensities is greatest. Figures 7(a) and 7(b) show this by comparing the mean standard deviation of pixel intensities $\bar{\sigma}_{px}$ with the standard error of the measured displacements in pixels ρ_{px} for both samples. The scatter in the trends is due to the asymmetry of the data presented in Fig. 6. This confirms that the mean standard deviation of patch pixel intensities provides a reliable indication of the potential PIV precision. The maximum achievable mean standard deviation of pixel intensities is lower for the sand than for the kaolin clay, as the sand is naturally darker than the untextured kaolin and thus the added material has less contrast relative to the background (demonstrated in Fig. 10).

Figures 8(a) and 8(b) compare the ASR and the corresponding standard errors for the clay and sand, respectively. Maximum

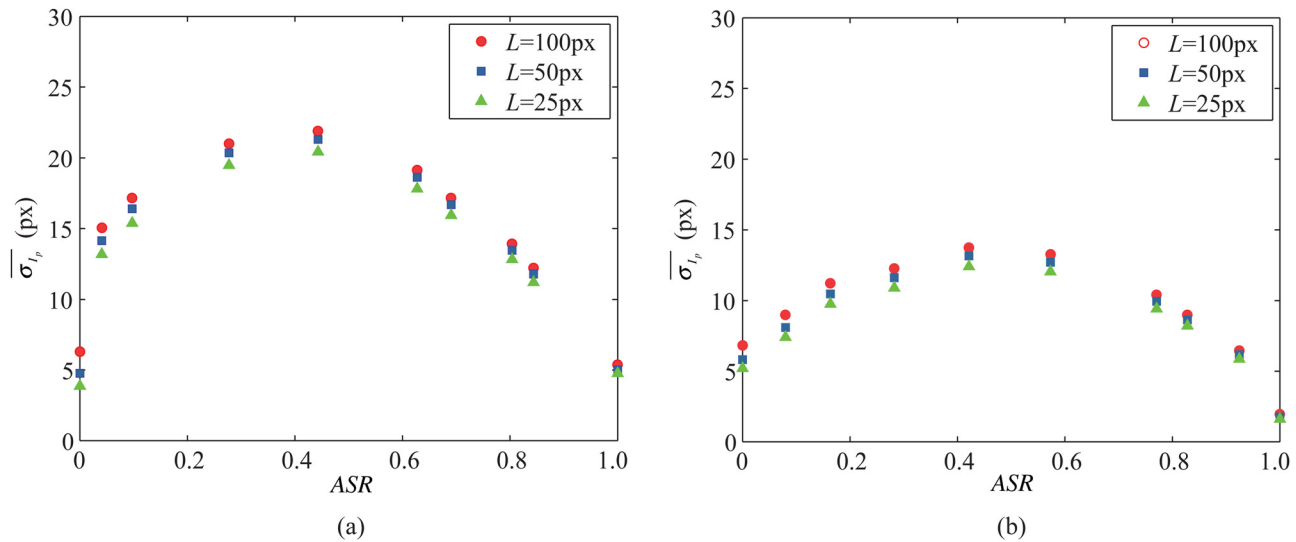


FIG. 6—Seeding density ratio versus the mean standard deviation of patch pixel intensities due to the addition of seeding on (a) kaolin clay and (b) silica sand.

precision is observed in the ASR range of 0.4 to 0.6 for all patch sizes tested. Comparing the gradients of improvement on either side of the optimal ASR range for the three patch sizes demonstrates that the precision increase due to seeding is greatest for the smaller patch sizes. Thus, as the measurement density (i.e., the fineness of the mesh of displacement measurements) is maximized, it becomes increasingly important to optimize the application of artificial seeding. A poor choice of seeding density can negate the benefits provided by improvements in camera technology such as higher image resolution.

Figures 7 and 8 demonstrate that artificially seeding the exposed plane of PIV models can lead to greatly improved precision in PIV computations, for both clay and sand. It is commonly accepted that the seeding of kaolin models with modeling flock or dyed sand is necessary in order to achieve reliable displacement measurement using PIV. However, it is also demonstrated here that a significant enhancement of PIV precision can also be gained

by means of artificially seeding sands. This is a technique that ought to be routinely applied in geotechnical physical modeling to maximize PIV measurement precision.

Optimizing Image Patch Size—The choice of patch size in a PIV analysis is inevitably a trade-off between achieving a finer mesh of displacement measurements (through the use of small patches) and increasing the accuracy of each displacement measurement (through the use of larger patches). To quantify the effect of patch size on displacement accuracy for the optimal artificial seeding ratios (0.44 for the kaolin clay and 0.58 for the sand according to Fig. 8), further comparative analyses were performed.

A mesh was generated using patch sizes in the range of 5 to 100 pixels, at intervals of 5 pixels, with 1000 different random patch locations. Apparent displacements were calculated for these

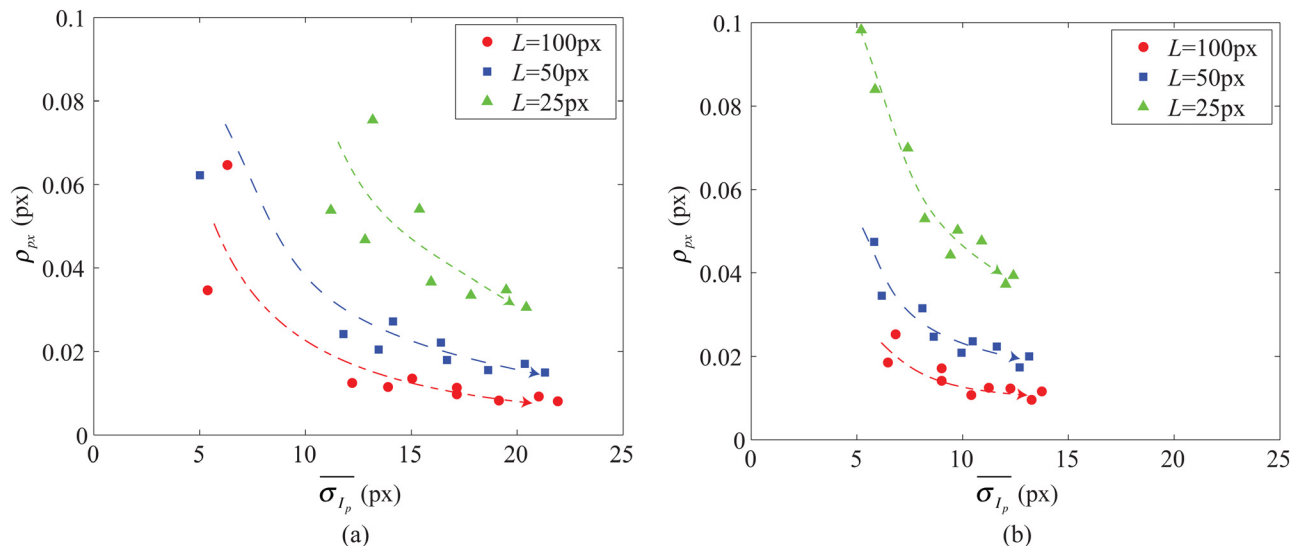


FIG. 7—Mean standard deviation of patch pixel intensities versus precision of PIV computation on (a) kaolin clay and (b) silica sand.

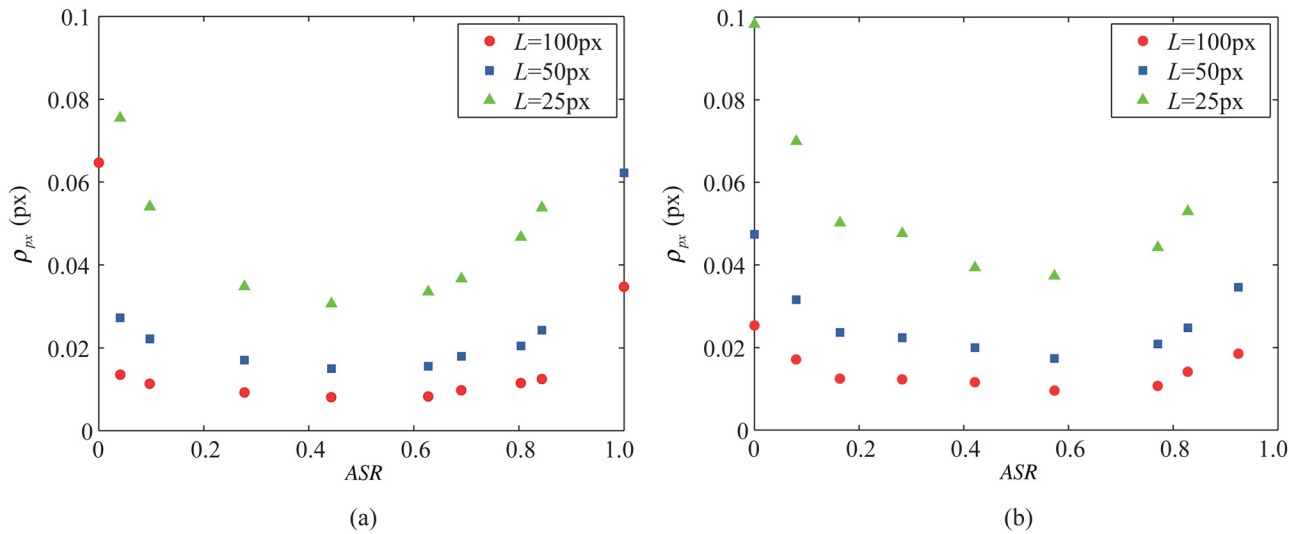


FIG. 8—Seeding density versus precision of PIV computation on (a) kaolin clay and (b) silica sand.

random meshes using the approach described earlier, allowing the standard errors to be assessed. To show the impact of optimizing the seeding on both kaolin clay and sand, the images with no seeding (ASR equal to zero) were also analyzed in the same way.

For comparison with the original GeoPIV calibration performed by White et al. (2003), the standard errors were normalized by the width of the images recorded (1760 pixels for the original calibration versus 2448 pixels for the AVT Prosilica GC2450C camera used here) such that the error was expressed as a fraction of the field of view. These normalized standard errors were compared to the empirical upper-bound precision fitted by White et al. (2003) to previous GeoPIV validation data. This expression represents a cautious estimate of PIV precision for real non-integer pixel displacements and is described by the following equation:

$$\rho_{n\text{-upper}} = \left(\frac{1}{W_{\text{pixel}}} \right) \cdot \left[\left(\frac{0.6}{L} \right) + \left(\frac{150000}{L^8} \right) \right] \quad (2)$$

where:

L = patch size ($6 < L < 50$ pixels were considered by White et al. [2003]), and W_{pixel} = image width in pixels.

Figure 9 presents the results of the patch-size calibration showing that for both kaolin clay and sand, the application of seeding to the exposed plane significantly improves PIV precision, causing the optimized precision to be better than the upper-bound curve of Eq 2. The improvement is quite marked; for example, for a 50-pixel patch the normalized standard error is reduced by a factor of 6.4 for the kaolin clay and 2.4 for the sand. There is greater improvement for the kaolin clay because this material exhibits very little natural brightness variation without artificial seeding.

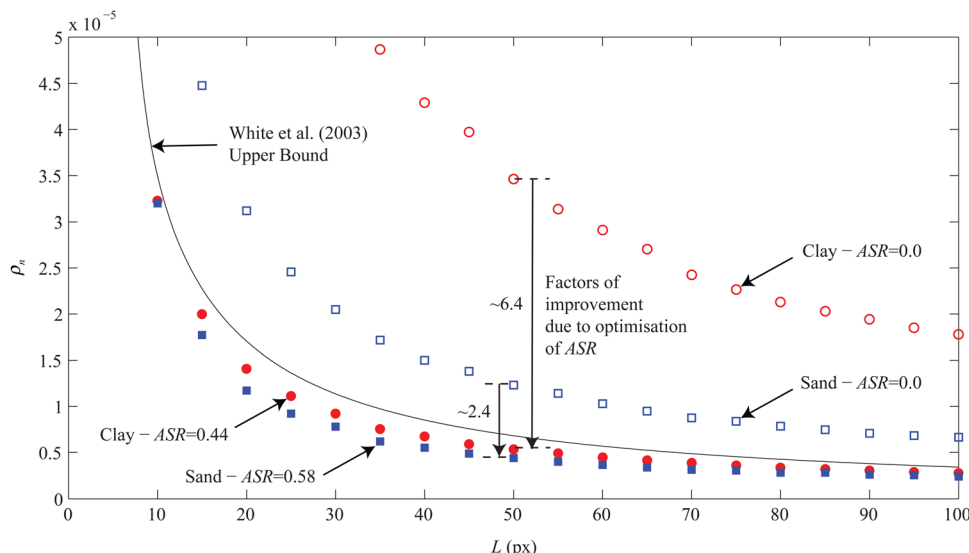


FIG. 9—Precision of PIV versus patch size for virgin and artificially seeded kaolin clay and silica sand.

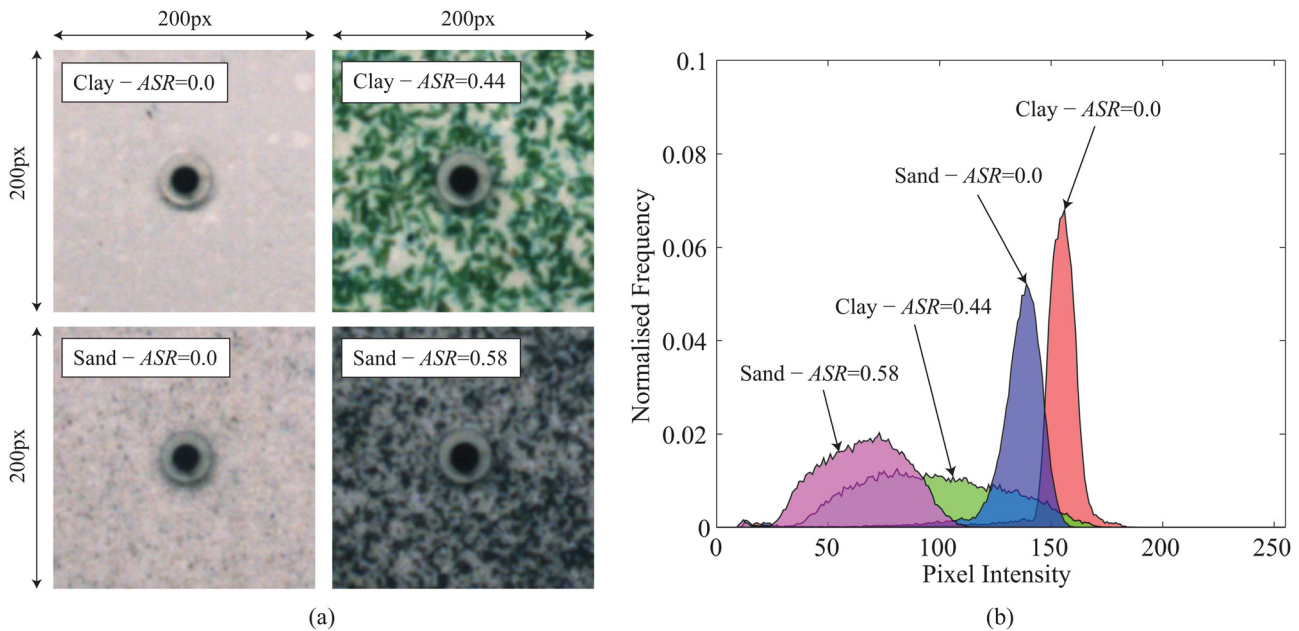


FIG. 10—Effect of artificial soil seeding: (a) visual impact; (b) increase in range of pixel intensities.

However, the significant improvement for sand, which is often used without artificial seeding, emphasizes the benefit of using an optimized quantity of artificial image texture.

The similar precision achieved from the texture optimization procedure for the kaolin clay and sand also demonstrates an additional benefit of the process. In models with multilayered strata, similar measurement precision can be attained throughout the imaged soil.

The visual effect of artificially seeding the exposed plane is shown by Fig. 10(a), which shows 200-pixel square regions bounding a 3-mm-diameter control point on the transparent acrylic viewing window for the cases with zero and optimized seeding for both clay and sand. Correspondingly, Fig. 10(b) is a normalized pixel intensity histogram with data for the four test regions of Fig. 10(a) overlaid. This illustrates that in the cases with no seeding, the distribution of pixel intensities is tightly grouped, leading to low $\bar{\sigma}_{px}$ and poor precision, whereas the addition of artificial seeding causes a wider distribution of pixel intensities, which leads to higher $\bar{\sigma}_{px}$ and improved PIV precision. This is more apparent for the optimally seeded clay than the sand, explaining why in Fig. 9 the optimally seeded clay (ASR = 0.44) exhibited slightly better precision than the optimally seeded sand (ASR = 0.58).

Relative Performance of the System

To give some context to the improvements the new system and techniques provide, the performance is here compared to that of previously reported image-based deformation measurement systems incorporating photogrammetry. Table 2 provides a summary of key performance metrics.

The video-based system of Taylor et al. (1998) is capable of relatively high frame rates, at the expense of resolution. This low

resolution limited the achievable normalized precision significantly. In contrast, the system described by White et al. (2003) featured significantly improved normalized precision, partly as a result of the increase in camera resolution, but mainly because of the advent of digital PIV and the use of image texture rather than target beads. However, the frame rate and thus the information capture rate were comparatively poor, and the system was suited only to slow quasi-static experiments. The system described by White et al. (2005) provided a significant improvement of both frame rate and resolution at the expense of camera control, as a simple g-level-activated shutter weight was relied upon to trigger image capture in flight. This increase in resolution, following White et al. (2003), led to a proportional increase in normalized precision. The recent improvements in camera technology, data communication systems, and lighting that have been described in this paper have allowed the advantages of all three systems to be combined into one. As a result, the system described here has fast capture rates similar to those reported by Taylor et al. (1998), comparable camera control to the system used by White et al. (2003), and the high resolution and normalized precision of the system described by White et al. (2005).

The two key performance indicators of these systems are (i) the rate at which displacement measurements can be gathered (strictly, this refers to *potential* measurements, as the PIV analysis is performed post hoc), which is the frame rate multiplied by the number of displacement vectors per frame, and (ii) the normalized precision of those measurements, expressed as a fraction of the field of view. These two metrics are shown as the penultimate two columns of Table 2. The quantities can even be combined into a single index by dividing the former by the latter, as shown in the final column of Table 2.

It is important to note that all of the recent PIV-based studies listed in Table 2 have given careful attention to the texture of the imaged soil, to maximize the system performance. The accuracy

TABLE 2—Summary of key performance metrics for selected image-based deformation measurement systems incorporating photogrammetry reported in the past 15 years.

| Reference | Camera | Frame Rate, Hz | Frame Resolution, Mpx | Capture Rate, Mpx/s | Information Control Interface | Data Interface or Storage | Target | Measurement Point Limitation | Maximum Measurements per Image N | Maximum Measurement Rate dN/dt , s^{-1} | Normalized Precision (Field of View) | Maximum Performance Index ^a |
|----------------------|-----------------------|----------------|-----------------------|---------------------|--|--|------------------|--------------------------------|----------------------------------|---|--------------------------------------|--|
| Taylor et al. (1998) | TELI CS3510 | 25 | 0.4 | 10 | Limited control via PCI image capture card | PCI and HDD storage on logging PC | Embedded targets | Number of Identifiable targets | ~900 | ~22 500 | 1/6720 to 1/4200 ^b | 1.5 E+08 |
| White et al. (2003) | Kodak DC280 | 0.033 | 2 | 0.066 | Custom PC software | USB and HDD storage on logging PC ^c | Image texture | Patch size L | ~3300 ($L = 25$ pixels) | 109 | 1/73 300 ^d | 8.0 E+06 |
| White et al. (2005) | Canon S40/50 | 0.5 | 3.8/5 | 1.9/2.5 | Shutter weight activated by g | On-board CompactFlash level storage | Image texture | Patch size L | ~6200/8000 ($L = 25$ pixels) | 4000 | 1/94 700 to 1/108 000 ^d | 4.3 E+08 |
| This investigation | AVT Prosilica GC2450C | 15 | 5 | 75 | Custom software control via gigabit Ethernet | Gigabit Ethernet and HDD storage on logging PC | Image texture | Patch size L | ~8000 ($L = 25$ pixels) | 120 000 | 1/108 000 ^d | 1.3 E+10 |

^aMaximum measurement rate/normalized precision.^bQuoted by Grant (1998).^cRefer to Take (2003).^dEstimated using Eq 2.

TABLE 3—Key parameters for example analysis of flat footing on sand overlying clay.

| Model Geometries | |
|------------------|--------------------------------------|
| H_s | 20 mm ^a /4 m ^b |
| D | 30 mm ^a /6 m ^b |
| Sand Properties | |
| I_D | 75% ^c |
| ϕ_{cv} | 31° ^d |
| ψ | 6.6° ^e |
| γ'_s | 10.6 kN/m ³ |
| D_{50} | 0.19 mm ^d |
| Clay Properties | |
| s_{u0} | 17.0 kPa ^f |
| ρ | 1.54 kPa/mf |

^aModel scale.

^bPrototype scale.

^cMeasured volumetrically.

^dAfter White et al. (2008).

^eEstimated following the procedure of Lee et al. (2009).

^fMeasured using T-bar penetrometer ($N_{T\text{-bar}} = 10.5$).

and precision of the displacement measurements are affected not only by the image capture and processing technology, but also by the way the soil sample is prepared and lit. This important message is reinforced by the detailed study of image texture reported in this paper. Experimentalists should give careful attention to these aspects through trial studies prior to embarking on the main testing program. High-quality image-based deformation measurements are not achieved simply by placing a camera in front of an existing experimental setup. Instead, we emphasize the need to optimize the soil texture and lighting.

Example Application

To demonstrate an application of the new PIV apparatus and texture optimization procedure, a 30-mm-wide flat footing was

pushed into a sample of dense sand ($I_D = 75\%$) overlying clay in the UWA drum centrifuge at an acceleration of 200 g. The main aim was to investigate the validity of the mechanisms proposed by Lee et al. (2009) to predict the peak penetration resistance (q_{peak}) during “punch-through,” which occurs when a foundation is loaded upon a thin, stiff layer of soil overlying a weaker layer.

Seeding was applied to the two layers using green flock for the clay and black dyed sand for the sand layer. The seeding densities were optimized through comparison with images of the optimum texture densities identified during the previously described optimization process. The texturing was then checked from images, and the ASR matched the target value determined previously.

During the test, the footing was displaced at rate of 0.254 mm/s, producing undrained penetration in the clay layer and drained penetration in the sand layer. Images were recorded during the test at 5 Hz, and PIV analysis was performed on the images using a patch size L of 50 pixels at a spacing s of 10 pixels. Such aggressive overlapping of the analysis patches was used to facilitate observation of the very fine shear strain feature detail that Lesniewska and Muir Wood (2009) demonstrated could be exposed using patch overlapping without impacting on the interpretation of the wider underlying mechanism of deformation. Other pertinent test details are summarized in Table 3.

Figure 11(a) is a plot of the measured penetration resistance with depth, and Fig. 11(b) is a magnified subplot of the same data illustrating the differing displacement increments measurable using the legacy and new PIV apparatus at the chosen test rate. The minimum displacement increment measurable using the new PIV apparatus was 0.002 D , which is equal to 0.012 m at prototype scale or 0.06 mm at model scale (i.e., $\sim 0.3D_{50}$). For the legacy apparatus, with a lower frame rate, the minimum measurable displacement increment was 0.02 D , which equates to 0.12 m at prototype scale or 0.6 mm at model scale. Figure 12 presents the corresponding PIV output for these two analyses, centered on the peak penetration resistance indicated in Fig. 11(b). The left-hand side of the line of symmetry of each of the subplots in Fig. 12 is an analysis representative of the performance of the new PIV

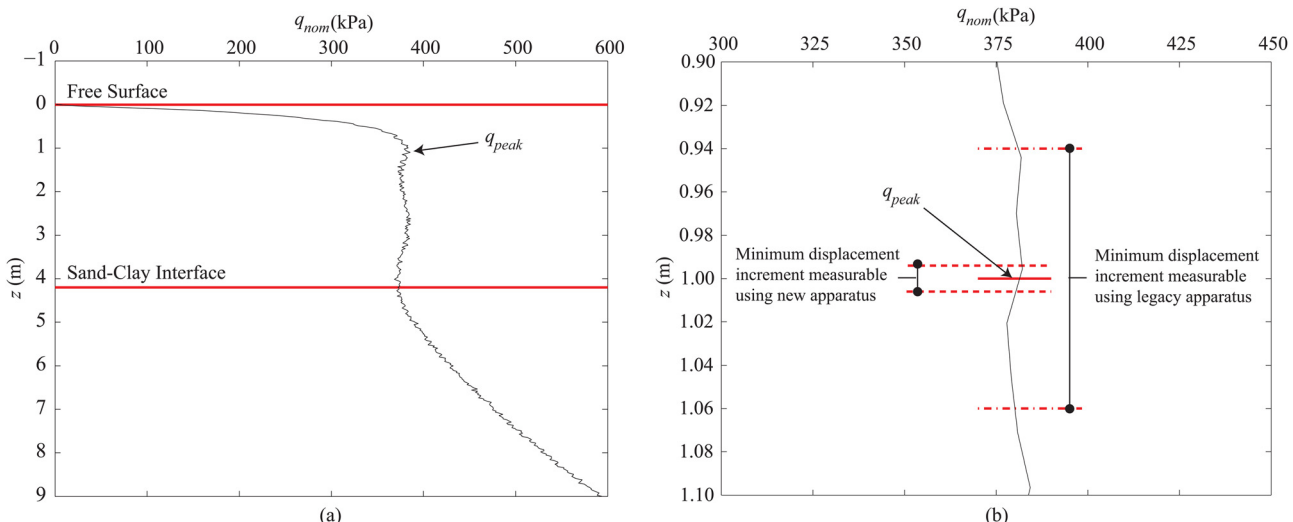


FIG. 11—Example PIV analysis: (a) nominal bearing pressure versus penetration response; (b) magnified response during mobilization of peak penetration resistance (q_{peak}) highlighting the minimum displacement increment measurable with the legacy and new PIV apparatus at the chosen test rate.

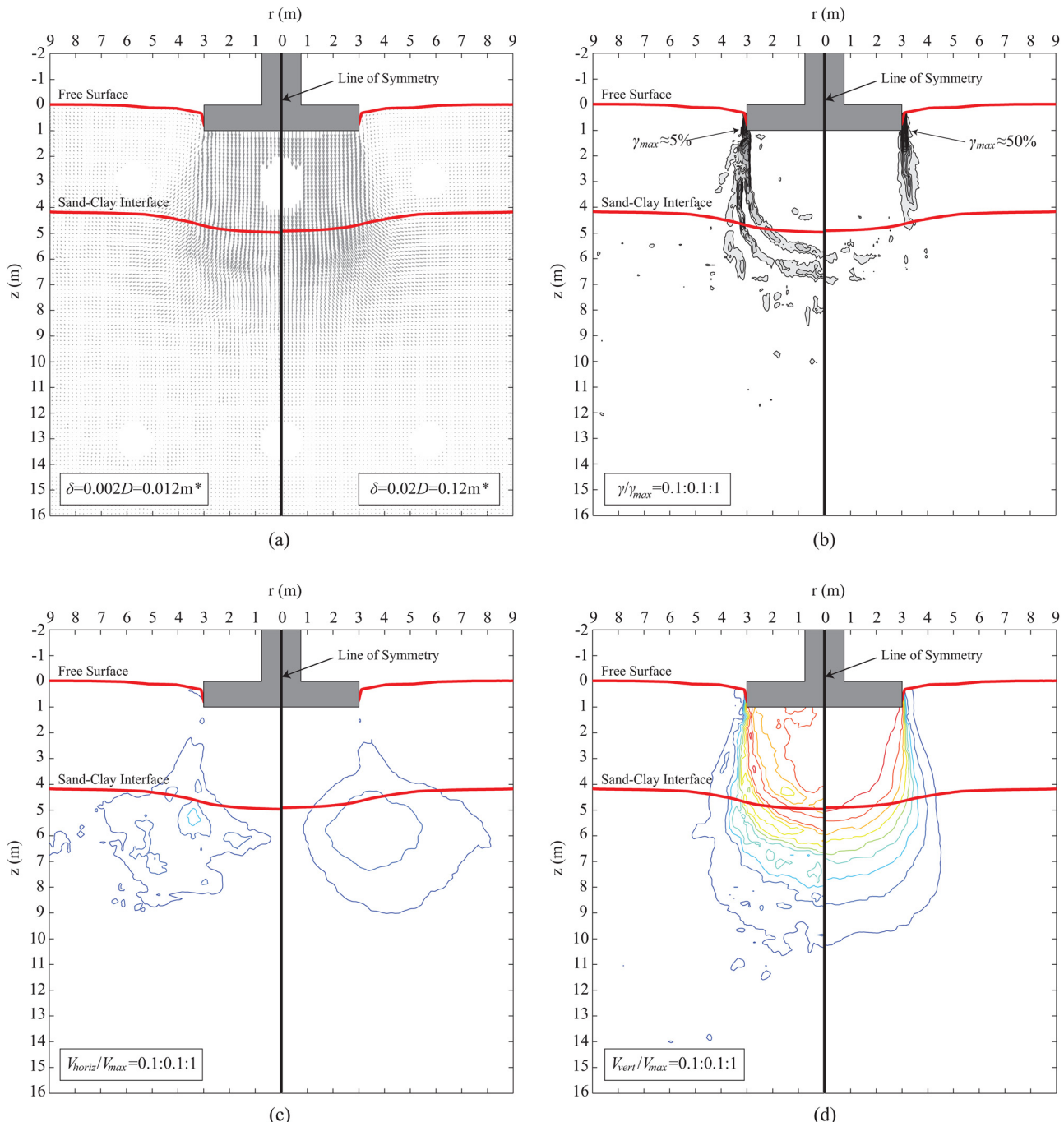


FIG. 12—Example PIV analysis: (a) normalized vectorial displacement fields; (b) normalized engineering shear strain fields (γ/γ_{\max}), (c) the normalized horizontal velocity fields ($V_{\text{horiz}}/V_{\max}$), and (d) the normalized vertical velocity fields (V_{vert}/V_{\max}). For two displacement increments with differing orders of magnitude. *Displacements given in prototype scale.

apparatus described in this paper. The right-hand sides of the lines of symmetry are mirrored plots of the same field of view for an analysis representative of the maximum performance of the legacy system described by White et al. (2005). Figure 12 presents (a) the normalized vectorial displacement fields (δ/δ_{\max}), (b) the normalized engineering shear strain fields (γ/γ_{\max}), (c) the normalized horizontal velocity fields ($V_{\text{horiz}}/V_{\max}$), and (d) the normalized vertical velocity fields (V_{vert}/V_{\max}). With the normalized fields plotted at intervals of 0.1, the interpretations are directly comparable.

The displacement, strain, and velocity fields derived over the larger footing displacement increment show a single straight shear zone, aligned almost vertically, bounding a rigid block of sand that is punching downward into the clay. The clay shows no distinct deformation features. This looks like the classical punch-through failure mechanism involving steady, continuous failure in a single zone of soil. The inclination of the shear zone can be used to infer an angle of dilation within the shearing soil of approximately 5° .

The displacement, strain, and velocity fields derived over the smaller footing displacement increment show a more complex picture. The deformation within the sand is divided into multiple finer shear zones, which fan out from the footing corner, spanning an enclosed angle of approximately 30°. Where each of these discontinuities reaches the clay layer, the discontinuity in the velocity field must continue—as required for compatibility—and these continuations extend as arcs into the clay layer. The fan of distinct discontinuities within the sand is more complex but theoretically more plausible than the single shear zone in the mirror image. The single zone suggests a constant dilation angle that is rather low for sand at 75 % relative density, whereas the fan implies a dilation angle that can be higher but which varies with shear strain, causing the shear zones to appear briefly before falling dormant. Similar patterns have been derived from trapdoor and retaining wall experiments in sand (Stone and Muir Wood, 1992).

The size of the localization features in Fig. 12(b) for the small displacement increment is approximately 2 mm at model scale, which is approximately $10D_{50}$. This size has significance with respect to strain localization features, as it is the size of a “homogeneously heterogeneous” shear zone (Muir Wood 2012). The increased capabilities of the new PIV apparatus, when coupled with the texture-optimization procedure proposed, leads to the PIV technique being able to identify not only macro- but also micro-scale deformation features occurring transiently at the particulate scale.

The larger displacement increment leads to time-integrated smearing of these details, particularly in the lower strain regions of the model (in both the clay layer and the sand layer). Consequently, the normalized velocity contours in Figs. 12(c) and 12(d) appear smoother for the larger displacement increment than for the small displacement increment analysis. This is because the improved data-capture rate of the new apparatus enables measurement of the very small displacements within the transient localizations of the homogeneously heterogeneous shear zone. This example demonstrates that it is not only the discretization of the PIV analysis domain (i.e., the adopted patch sizes) that influences shear strain field detail (Lesniewska and Muir Wood 2009), but also the displacement increment over which the computation is performed.

In this example, the deformations calculated using the capabilities of the legacy system reveal a simple failure mode that can be back-analyzed using a single slip plane and a limit equilibrium-type calculation (e.g., Lee et al. 2009). The more detailed results from the new system show that this answer is overly simple and the true response does not involve a single slip plane. The higher frame rate and improved spatial precision of the new system reveal successive localizations beneath the footing that raise fascinating questions about progressive failure and scale effects in miniature models, and which provide more truthful validation data for back-analyses.

Conclusions

Geotechnical engineering has made extensive use of PIV techniques during the past 15 years to provide improved image-based

measurements of deformation in model tests and element tests. Unlike the fluid mechanics discipline, from which PIV emerged, geotechnical engineering is often concerned with very small strain levels. This has led to the development of techniques to refine the precision of PIV-based deformation measurements through improvements in both the experimental procedures and the imaging hardware and software.

This paper describes advances that provide improved image-based deformation measurements of geotechnical model tests. These include (i) new technologies of image control, capture, and transfer that overcome the challenges of the centrifuge environment; (ii) new methods for quantifying and optimizing the image texture that is added to the observed soil plane; and (iii) new methods for optimizing the manner in which the image is subdivided into discrete displacement measurements. The improved performance provided by these advances is quantified. In summary, the present system gathers measurement points approximately 1000 times more rapidly than the earlier incarnation described by White et al. (2003), and new techniques of texture quantification allow the optimal measurement precision to be achieved—typically 1/100 000th of the width of the field of view.

An example application is used to illustrate that this performance is sufficient to identify both macroscopic and microscopic features from the same series of images of a boundary value problem. In this case, the failure mechanism around a footing is identified, including local irregular strain patterns within the evolving shear zone.

Acknowledgments

The work forms part of the activities of the Centre for Offshore Foundation Systems (COFS) at the University of Western Australia, which is supported by the Lloyd’s Register Foundation as a Centre of Excellence and is a node of the Australian Research Council (ARC) Centre of Excellence in Geotechnical Science and Engineering. The second writer is supported by an ARC Future Fellowship and holds the Shell Energy and Minerals Institute (EMI) Chair in Offshore Engineering.

References

- Andrawes, K. Z. and Butterfield, R., 1973, “The Measurement of Planar Displacements of Sand Grains,” *Géotechnique*, Vol. 23(5), pp. 571–576.
- Butterfield, R., Harkness, R. M., and Andrawes, K. Z., 1970, “A Stereo-Photogrammetric Technique for Measuring Displacement Fields,” *Géotechnique*, Vol. 20(3), pp. 308–314.
- Cilingir, U. and Madabhushi, G., 2010, “Effect of Depth on Seismic Response of Circular Tunnels,” *Can. Geotech. J.*, Vol. 48(1), pp. 117–127.
- Gaudin, C., Clukey, E. C., Garnier, J., and Phillips, R., 2010a, “New Frontiers for Centrifuge Modelling in Offshore Geotechnics,” Invited Keynote Lecture, *2nd International Symposium on Frontiers in Offshore Geotechnics*, Perth, Australia, Nov 8–10, 2010, University of Western Australia (UWA), pp. 155–188.
- Gaudin, C., White, D. J., Boylan, N., Breen, J., Brown, T., and De Catania, S., 2010b, “A Miniature High Speed Wireless Data

- Acquisition System for Geotechnical Centrifuges," *7th International Conference on Physical Modelling in Geotechnics (ICPMG)* (CD-ROM), Taylor & Francis, London, pp. 229–234.
- Grant, R., 1998, "Movements around a Tunnel in Two-layer Ground," Ph.D. thesis, City University, London.
- Knappett, J. A., Haigh, S. K., and Madabhushi, S. P. G., 2006, "Mechanisms of Failure for Shallow Foundations Under Earthquake Loading," *Soil Dyn. Earthquake Eng.*, Vol. 26(2–4), pp. 91–102.
- Lee, K. K., Randolph, M. F., and Cassidy, M. J., 2009, "New Simplified Conceptual Model for Spudcan Foundations on Sand Overlying Clay Soils," Offshore Technology Conference OTC20012, Houston, TX, May 4–7, OTC.
- Lesniewska, D. and Muir Wood, D. M., 2009, "Observations of Stresses and Strains in a Granular Material," *J. Eng. Mech.*, Vol. 135(9), pp. 1038–1054.
- Muir Wood, D. M., 2012, "Heterogeneity and Soil Element Testing," *Géotechnique Lett.*, Vol. 2, pp. 101–106.
- Okamura, M., Matsuo, O., and Tamoto, S., 2001, "A High Frame Rate Image Acquisition System for Dynamic Centrifuge Tests," *Int. J. Phys. Modell. Geotech.*, Vol. 1(1), pp. 71–76.
- Pan, B., Qian, K., Xie, H., and Asundi, A., 2009, "Two-dimensional Digital Image Correlation for In-plane Displacement and Strain Measurement: A Review," *Meas. Sci. Technol.*, Vol. 20(6), 62001.
- Raffel, M., Willert, C., Wereley, S., and Kompenhaus, J., 2007, *Particle Image Velocimetry—A Practical Guide*, Springer-Verlag, Berlin.
- Stanier, S. A., Black, J. A., and Hird, C. C., 2012, "Enhancing Accuracy and Precision of Transparent Synthetic Soil Modelling," *Int. J. Phys. Modell. Geotech.*, Vol. 12(4), pp. 162–175.
- Stewart, D. P., Boyle, R. S., and Randolph, M. F., 1998, "Experience With a New Drum Centrifuge," *Proceedings of the International Conference Centrifuge 98*, Vol. 1, Tokyo, Japan, Sept 23–25, Tokyo Institute of Technology, Tokoyo, Japan, pp. 35–40.
- Stone, K. J. L. and Muir Wood, D. M., 1992, "Effects of Dilatancy and Particle Size Observed in Model Tests on Sand," *Soils Found.*, Vol. 32(4), pp. 43–57.
- Sutton, M. A., Oreu, J.-J., and Schreier, H. W., 2009, *Image Correlation for Shape, Motion and Deformation Measurements*, Spring Science and Business Media, New York.
- Take, W., 2003, "The Influence of Seasonal Moisture Cycles on Clay Slopes," Ph.D. thesis, University of Cambridge, Cambridge, UK.
- Take, W. and Bolton, M. D., 2011, "Seasonal Ratcheting and Softening in Clay Slopes, Leading to First-time Failure," *Géotechnique*, Vol. 61(9), pp. 757–769.
- Taylor, R., Grant, R., Robson, S., and Kuwano, J., 1998, "An Image Analysis System for Determining Plane and 3D Displacements in Soil Models," *Proceedings of the International Conference on Centrifuge Modelling, Centrifuge'98*, Vol. 1, Tokyo, Japan, Sept 23–25, Tokyo Institute of Technology, Tokoyo, Japan, pp. 73–78.
- White, D. J., 2008, "Contributions to Géotechnique 1948–2008: Physical Modelling," *Géotechnique*, Vol. 58(5), pp. 413–421.
- White, D. J., Randolph, M. F., and Thompson, B., 2005, "An Image-based Deformation Measurement System for the Geotechnical Centrifuge," *Int. J. Phys. Modell. Geotech.*, Vol. 3, pp. 1–12.
- White, D. J. and Take, W. A., 2002, "GeoPIV: Particle Image Velocimetry (PIV) Software for Use in Geotechnical Testing," *Technical Report D-SOILS-TR322*, Cambridge University Engineering Department, Cambridge University, Cambridge, UK.
- White, D. J. and Take, W. A., 2005, "Discussion on: Application of Particle Image Velocimetry (PIV) in Centrifuge Testing of Uniform Clay by Zhang Y. D., Tan T. S. & Leung C. F.," *Int. J. Phys. Modell. Geotech.*, Vol. 5(4), pp. 27–31.
- White, D. J., Take, W., and Bolton, M., 2003, "Soil Deformation Measurement Using Particle Image Velocimetry (PIV) and Photogrammetry," *Géotechnique*, Vol. 53(7), pp. 619–631.
- White, D. J., Teh, K. L., Leung, C. F., and Chow, Y. K., 2008, "A Comparison of the Bearing Capacity of Flat and Conical Circular Foundations on Sand," *Géotechnique*, Vol. 58(10), pp. 781–792.